

# On the variability of flocculated particle characteristics in a shallow estuary

Galen Egan <sup>1,2</sup>, Grace Chang <sup>3</sup>, Andrew J. Manning <sup>1,4</sup>, Stephen Monismith <sup>1</sup>,  
and Oliver Fringer <sup>1</sup>

<sup>1</sup>Stanford University, Department of Civil and Environmental Engineering, 473 Via Ortega, Stanford, CA,  
94035

<sup>2</sup>Sofar Ocean Technologies, Shed B, Pier 50, San Francisco, CA, 94158

<sup>3</sup>Integral Consulting Inc., 200 Washington St Suite 201, Santa Cruz, CA, 95060

<sup>4</sup>HR Wallingford Ltd, Coasts and Oceans Group, Wallingford, UK

## Key Points:

- Wave shear stress is the strongest contributor to flocc breakup in our field data.
- Water temperature likely serves as a proxy measurement for biological processes that encourage flocc growth during productive periods.
- Sediment transport modeling parameters such as fractal dimension and inverse turbulent Schmidt number vary seasonally.

## Abstract

We conducted field work in South San Francisco Bay to examine cohesive sediment flocculation dynamics in a shallow, wave- and current-driven estuarine environment. Drawing on data collected using a suite of acoustic and optical instrumentation over three distinct seasons, we found that the factors driving floc size variability differed substantially when comparing locally-sourced sediment (i.e., through wave-driven resuspension) to suspended sediment advected from upstream. Statistical analysis of our extensive field data revealed additional seasonal variability in these trends, with wave stress promoting floc breakup during the summer and winter months, and biological processes encouraging floc growth during the spring productive period. Combining these data with fractal dimension estimates, we found that seasonally-varying floc composition can lead to differences in floc settling velocity by a factor of approximately two to five for a given floc size. Finally, by analyzing co-located turbulence and sediment flux measurements from the bottom boundary layer, we present evidence that the relationship between floc size and the inverse turbulent Schmidt number varies with floc structure. These results can be used to inform sediment transport modeling parameterizations in estuarine environments.

## Plain Language Summary

Sediment is a ubiquitous natural material that comprises everything from the earth beneath our feet to the sandy beaches along our coasts. Manmade infrastructure and natural ecosystems alike depend on adequate supplies of sediment for their stability. Therefore, it is critical that we understand how sediment moves through coastal environments. One of the greatest challenges when predicting sediment transport in estuaries and coastal regions is accurately depicting how quickly sediment falls through the water due to gravity. This seemingly simple process is complicated by the tendency for individual sediment particles to stick together, or “flocculate,” which can cause them to settle more quickly. In this study, we took measurements in South San Francisco Bay to understand what natural processes exert the strongest influence on sediment flocculation, and how that flocculation affects sediment settling. We found that settling behavior is very different from season to season, but that the effects of waves and biological material in the water can be particularly impactful in determining whether or not sediment particles will stick to each other.

## 1 Introduction

The properties of aggregated marine particles, or flocs, exert an influence on numerous estuarine processes (Dyer, 1989). For example, suspended sediment settling fluxes are a strong function of both particle size and composition (Manning & Bass, 2006), and predicting these fluxes is critical as sea level rise drives unprecedented morphological changes along coastlines and within estuaries worldwide (Prandle & Lane, 2015). Additionally, the transport of contaminants that readily adhere to sediment aggregates are largely determined by the transport properties of the aggregates themselves (Lick, 2008; Mehta et al., 2014), necessitating a comprehensive understanding of how flocs move and evolve in wavy, turbulent flows. Rates of photosynthesis and the potential for algal blooms, too, are controlled by the vertical distribution of particles throughout the water column (Cloern, 1996), which itself depends on the interplay between hydrodynamic forcing and particle characteristics.

Numerical models often simulate the transport of flocs by separating them into discrete size classes (James et al., 2010; Soulsby et al., 2013; Verney et al., 2009). Each size class is then treated as an Eulerian concentration field with a superimposed settling velocity,  $w_s$ , assumed to follow Stokes Law (Stokes et al., 1851),

$$w_s = \frac{(\rho_f - \rho_0)gd_f^2}{18\mu}. \quad (1)$$

Here,  $\rho_f$  is the floc density,  $\rho_0$  is the background fluid density,  $g$  is acceleration due to gravity,  $d_f$  is the floc diameter, and  $\mu$  is the dynamic viscosity of water. The floc diameter varies with aggregation and breakup, ranging from the primary particle size,  $d_p$ , to the Kolmogorov scale,  $\eta$  (Kolmogorov, 1941; Eisma, 1986). These size variations further affect the floc density, which can be described following Kranenburg (1994) as

$$\rho_f = \rho_0 + (\rho_p - \rho_0) \left( \frac{d_f}{d_p} \right)^{n_f-3}, \quad (2)$$

where  $\rho_p$  is the primary particle density, and  $n_f$  is the floc fractal dimension. A commonly used value for the fractal dimension is  $n_f = 2.1$ , but field studies have shown that this can vary widely (Dyer & Manning, 1999). Taking variations in floc density and fractal dimension into account, Khelifa and Hill (2006) proposed a more complex model for the floc settling velocity,

$$w_s = \frac{1}{18} \theta g \frac{\rho_p - \rho_0}{\mu} d_p^{3-n_f} \frac{d_f^{n_f-1}}{1 + 0.15 \text{Re}^{0.687}} \phi. \quad (3)$$

Here,  $\text{Re} = \frac{w_s d_f}{\nu}$  is the particle Reynolds number,  $\theta$  is a dimensionless floc shape factor, and  $\phi$  describes the size distribution of floc-forming primary particles. Though Equation 3 can account for a wide range of particle population characteristics, recent high-resolution imaging studies have shown that fractal theory does not adequately describe the structure of natural flocs (Spencer et al., 2021). Nevertheless, casting the evolution of settling velocity as a power law with coefficients derived from regressions to observational data is a widely-used and pragmatic approach, so we will analyze floc settling within this framework despite the flaws of the fractal assumption.

Not only do flocs settle under the influence of gravity, but their turbulent diffusivity differs from that of a passive tracer. This is parameterized through the inverse turbulent Schmidt number,

$$\beta = \frac{\kappa_T}{\nu_T}, \quad (4)$$

where  $\kappa_T$  is the turbulent floc diffusivity and  $\nu_T$  is the turbulent eddy viscosity. Numerous studies have examined how  $\beta$  evolves with flow and sediment properties (see Gualtieri et al. (2017) for a review), with general agreement that  $\beta$  decreases with increasing turbulence (as particles cannot fully track the turbulent fluctuations) and decreasing particle settling velocity. However, other results (e.g., Lees, 1981; Brand et al., 2010) have proven inconclusive regarding the effects of particle properties on  $\beta$ , so in practical sediment transport modeling applications where a sediment diffusivity is required, a constant value of  $\beta = 1$  is often prescribed.

Despite the ubiquity of suspended marine particles, the precise rates at which they flocculate and break up in the environment, and thus their transport properties, remain difficult to quantify. This is primarily due to the large number of flocculation mechanisms and the vast range of relevant spatiotemporal scales, which span turbulent particle-scale dynamics to seasonally varying estuary-scale conditions. Laboratory experiments have been used extensively to examine flocculation, but are generally conducted in jars or settling columns, which cannot recreate field-scale conditions. Nevertheless, a great deal has been learned from these studies. For example, reduced pH and increased salinity have both been shown to encourage floc growth (Mietta et al., 2009). Water column biology affects flocculation too, as the presence of extracellular polymeric substances (EPS) can act as a glue holding discrete sediment particles together (Eisma, 1986; Tolhurst et al., 2002). In terms of physical mechanisms, neither Brownian motion (McCave, 1984) nor

differential settling (Stolzenbach & Elimelech, 1994) are expected to contribute significantly to flocculation. Turbulence can have competing effects, as it can either increase flocculation by enhancing particle collision rates, or decrease it through shear-induced breakup (Van Leussen, 1997; Manning & Dyer, 1999; Winterwerp, 1998).

These particle dynamics have been studied numerically as well. Treating flocs as self-similar fractal entities, Winterwerp (2002) proposed an Eulerian model for the floc number density accounting for turbulent shear and hindered settling processes. Expanding on that work, Son and Hsu (2011) were able to better represent field data with a numerical model when they accounted for variable fractal dimension and floc yield strength. One recent study has shown particular promise by directly resolving individual particles and examining their flocculation dynamics through a first-principles cohesion function (Vowinckel et al., 2019), though as of yet this approach is limited to quiescent flows.

Field deployments using a range of instrumentation have also been used to study flocculation, and have an inherent advantage over laboratory and numerical work in that the particle dynamics are affected by the full range of physical, chemical, and biological forcing mechanisms. Heffler et al. (1991) developed an *in situ* floc camera termed an FCA to simultaneously measure floc size, shape, and settling velocity. The FCA has been used to elucidate the evolution of floc properties like effective density over timescales ranging from minutes to seasons (Syvitski & Hutton, 1996). Additional FCA studies have found significant variability in floc size–density relationships (Hill et al., 1998), potentially due to natural variability in particle composition. Similar *in situ* floc cameras have been developed as well (e.g., the Benthos 373 of Milligan, 1996), with studies showing that higher suspended sediment concentration (SSC) can encourage flocculation (Hill et al., 2000). More recent studies have augmented floc settling column video data using advanced image processing techniques, further reducing uncertainty in fractal dimension and effective density estimates (Smith & Friedrichs, 2011, 2015).

Another *in situ* video imaging device (and the one used in this study) is the INSSEV-LF (In Situ Settling Velocity - Laboratory Spectral Flocculation Characteristics; Manning et al. (2007, 2017)), which has been used to track the evolution of floc size and fractal dimension with turbulent shear and SSC (Dyer & Manning, 1999). Results showed that weak shear enhances flocculation while stronger shear disrupts it, and that increased SSC tends to increase the floc fractal dimension. Another INSSEV-LF study observed mixed

sand-mud flocs, casting doubt on the ability of self-similar fractal models to adequately describe flocculation dynamics (Manning & Schoellhamer, 2013). The authors also postulated that this type of mixed floc was encouraged by the presence of sticky organic polymers that arise during phytoplankton blooms, indicating that biological activity could play a major role in determining sediment floc composition.

Though video-based systems like the INSSEV-LF provide simultaneous measurements of particle size and settling velocity, moored particle size analyzers such as the LISST (Laser In-Situ Scattering and Transmissometry; Sequoia Scientific) used in conjunction with absorption and attenuation meters (e.g., WetLabs *ac-9*) can provide superior temporal sampling resolution when measuring particle size and composition. Following the methods of Roesler et al. (1989), *ac-9* measurements can reveal information on particle composition by analyzing absorption and attenuation spectra. In terms of measuring particle size distributions (PSDs), LISSTs have been used extensively, allowing for quantification of mean particle size, along with higher order moments and their evolution over time (Agrawal & Pottsmith, 2000). For an extensive review of the utility and limitations of these types of optical measurements, see Boss et al. (2018).

In this study, we present results from three field campaigns studying flocculated particle characteristics in South San Francisco Bay, California, USA. By deploying a suite of moored optical instruments in conjunction with high resolution turbulence measurements and INSSEV-LF sampling, we examined variability in particle properties over three seasons as a function of local physical, chemical, and biological properties of the water column. Results point to two distinct regimes of suspended sediment: locally sourced via resuspension and non-locally sourced via advection. A Least Absolute Shrinkage and Selection Operator (LASSO) regression analysis was able to better-predict floc size in the resuspension regime, with floc size negatively correlated to wave strength in the summer and winter, and positively correlated to water temperature during the spring phytoplankton bloom period. The positive correlation to temperature (which increased in strength with chlorophyll concentration) indicates a strong biological control on floc size, which we show has implications for particle settling velocity parameterizations in numerical sediment transport models.

## 2 Methods

### 2.1 Field Deployments

The dataset presented herein was collected as part of a larger study examining cohesive sediment erosion and boundary layer dynamics in South San Francisco Bay. Comprehensive descriptions of the study site and field deployments can be found in our previous papers analyzing other aspects of the data (Egan et al., 2019; Egan, Manning, et al., 2020; Egan, Chang, et al., 2020; Egan et al., 2021). The details most pertinent to this manuscript will be repeated here for clarity.

Data were collected on the shallow (1.5 m mean lower low water, 2 m tidal range) shoals of South San Francisco Bay from 07/17/2018 - 08/15/2018 (summer deployment), 01/10/2019 - 02/07/2019 (winter deployment), and 04/17/2019 - 05/15/2019 (spring deployment). Our primary platform contained a suite of optical instruments, including two Sequoia Scientific Inc. LISST-100x's mounted at 15 and 45 centimeters above the bed (cmab), respectively. Each LISST measured suspended sediment particle size distributions (PSDs) once per hour. The platform also held an SBE *ac*-9 mounted at 15 cmab and an SBE *ac*-s mounted at 45 cmab. Both sensors measured spectral absorption and attenuation once per hour, coinciding with LISST measurements, with the *ac*-9 providing data at 9 wavelengths, and the *ac*-s providing data at 87 wavelengths. At both 15 and 45 cmab, we mounted an SBE ECO BB backscatter sensor and ECO FL fluorometer, which took measurements every 20 minutes. Over the course of the summer and spring deployments, we recovered and redeployed the platform twice to clean the optical windows on each instrument. During the winter, biofouling was less severe so the instruments were cleaned once.

Approximately 30 m from the optics platform, we deployed a sawhorse frame containing acoustic Doppler velocimeters (ADV) at 5, 15, and 45 cmab, and a Vectrino Profiler (Vectrino) with its measurement volume overlapping the bed from 0–1.5 cmab. The ADVs sampled the 3D velocity, pressure, and acoustic backscatter at 8 Hz for 14 minutes each hour, and the Vectrino sampled the 3D velocity and acoustic backscatter over 30 1 mm-spaced vertical bins at 64 Hz for 12 minutes each hour in the summer, and 14 minutes each hour in the spring (it did not sample in the winter due to a battery failure). The platform also held an RBR Bottom Pressure Recorder (BPR) mounted at 100 cmab sampling pressure at 6 Hz, and an SBE37 CTD mounted at 67 cmab measuring

salinity, temperature, and pressure once per minute. Approximately 10 m from the main platform, we mounted an upward-facing Aquadopp acoustic Doppler profiler (ADP) on an auxiliary plate, which measured vertical current profiles every three minutes based on 72 seconds of averaging.

The day following platform deployment each season, we conducted INSSEV-LF sampling adjacent to the sawhorse platform to simultaneously measure floc size and settling velocity within the bottom boundary layer. Flocs were sampled from within 2 cm of the sediment bed using a custom pipette fitted within a 3D-printed halo frame to prevent direct contact between the pipette and the bed. Samples were then immediately deposited into the INSSEV-LF settling chamber. Sampling was repeated every 15 minutes for approximately 8 hours in order to capture a wide range of tidal current magnitudes. The pipette/halo sampler was tested in laboratory flume dye study prior to the field work to ensure that sampling did not significantly disturb the flow.

## 2.2 Data Processing

Though LISSTs were deployed at two measurement heights, we did not find significant variability in the PSDs between 15 and 45 cmab. Therefore, our analysis will focus on the near-bed data at 15 cmab. Specific data processing methods for calculating hydrodynamic variables can be found in our previous papers and here we will analyze particle properties as a function of: bottom wave-orbital velocity,  $u_b$ , mean current velocity in the principal tidal direction,  $\bar{u}$ , and turbulent kinetic energy (TKE) dissipation rate,  $\epsilon$ , each of which were calculated using 15 cmab ADV data. The ADV and Vectrino data also provided estimates of the mean sediment concentration,  $\bar{c}$ , by calibrating acoustic backscatter readings against known concentrations of suspended sediment in the lab, using mud collected from the study site. Calibration curves can be found in Egan, Manning, et al. (2020).

Optical sensors were calibrated prior to each deployment following manufacturer-recommended protocols. The LISSTs and *ac*-meters were calibrated with MilliQ water. Chl-*a* concentration from ECO-fluorometer measurements were factory calibrated using a mono-culture of the diatom, *Thalassiosira weissflogii*. It is recognized that Chl-*a* containing material at the study site is not composed of strictly *Thalassiosira weissflogii* and therefore absolute concentrations of Chl-*a* from fluorescence techniques may not be ac-



curate. However, the derived variability of Chl-*a* can be considered true. ECO BB and ECO FL sensors were corrected to dark count calibrations conducted prior to deployment; any deviation from factory calibrations resulted in new dark counts.

Optical properties and products were analyzed according to the literature or factory recommended procedures. Backscattering coefficients were derived from ECO BB sensors according to Boss and Pegau (2001) after subtraction of backscattering by pure seawater (Zhang et al., 2009). The *ac*-9 and *ac*-s corrections for temperature and salinity effects were applied to absorption coefficients according to Zaneveld and Pegau (1993) and Sullivan et al. (2006). The specific absorption ratios we report, where the subscript indicates wavelength, are  $a_{676}/a_{650}$  (Chl-*a* absorption peak), and  $a_{450}/a_{676}$  and  $a_{412}/a_{650}$ , both of which indicate increased detrital and/or dissolved material relative to phytoplankton. LISST data were processed using the manufacturer-provided MATLAB processing code; additional processing involved removal of data affected by scintillation. Scintillation is a known issue with LISST data, where laser light may defocus and cause erroneous (spiky) data at the largest or smallest particle sizes. These effects were identified by comparing volume PSD data across size bins. Erroneous data were identified as data spikes of 40% or greater across consecutive size bins at the five smallest and five largest instrument rings. Once these data were removed, mean particle size was calculated from the resulting volumetric distribution measurements using the manufacturer-provided scripts.

INSSEV-LF high resolution video floc measurements were processed following the methods described by Manning et al. (2017) in order to produce spectra of floc size and settling velocity. Floc fractal dimensions were calculated following the methods of Kranenburg (1994) and Winterwerp (1998).

Combining hydrodynamic and sediment data, we also calculated the inverse turbulent Schmidt number ( $\beta$ , Equation 4) using Vectrino Profiler data. The turbulent Reynolds stress,  $\overline{u'w'}$ , was estimated with the phase method (Bricker & Monismith, 2007), and the turbulent sediment flux,  $\overline{c'w'}$ , was calculated as the covariance between the Vectrino sediment concentration and vertical velocity. Combining the fluxes with vertical gradients of the mean profiles, the inverse turbulent Schmidt number is given by

$$\beta = \frac{\overline{c'w'} \left( \frac{\partial \overline{c}}{\partial z} \right)^{-1}}{\overline{u'w'} \left( \frac{\partial \overline{u}}{\partial z} \right)^{-1}}. \quad (5)$$

This produces a profile of  $\beta$ , which we averaged over the range 0.3–1.0 cmab, neglecting the low signal-to-noise ratio portions at the top of the profile and near the bed (Koca et al., 2017).

### 3 Results & Discussion

#### 3.1 Site conditions

A wide range of estuarine conditions were sampled over the course of the three deployments, as shown by the time series data in Figure 1. During the summer, diurnal northwesterly winds resulted in strong wave-orbital velocities each afternoon (Figure 1a). The spring wave conditions were similar to the summer, though they contrasted with the winter deployment, when strong waves were restricted to isolated storm events. Mixed semidiurnal tidal currents were broadly similar for all three deployments, with peak depth-averaged velocities nearing  $50 \text{ cm s}^{-1}$  (not shown). Water temperatures were highest in the summer followed by spring and winter (Figure 1b). Salinity was highest in the summer and comparable (though steadily decreasing) throughout winter, with far lower values in the spring (Figure 1c). Chlorophyll-*a* fluorescence was highest at the beginning of the spring deployment, lowest throughout the winter, and reached moderate levels coinciding with the peak water temperature every afternoon in the summer (Figure 1d). Turning to particle properties, the summer and winter deployments saw floc size inversely correlated to wave strength (Figure 1e). In the spring,  $d_f$  was generally larger, especially during the productive period at the beginning of the deployment. In Section 3.3, variations in floc size will be discussed and analyzed in the context of the diverse set of physical, chemical, and biological conditions observed during the field campaigns.

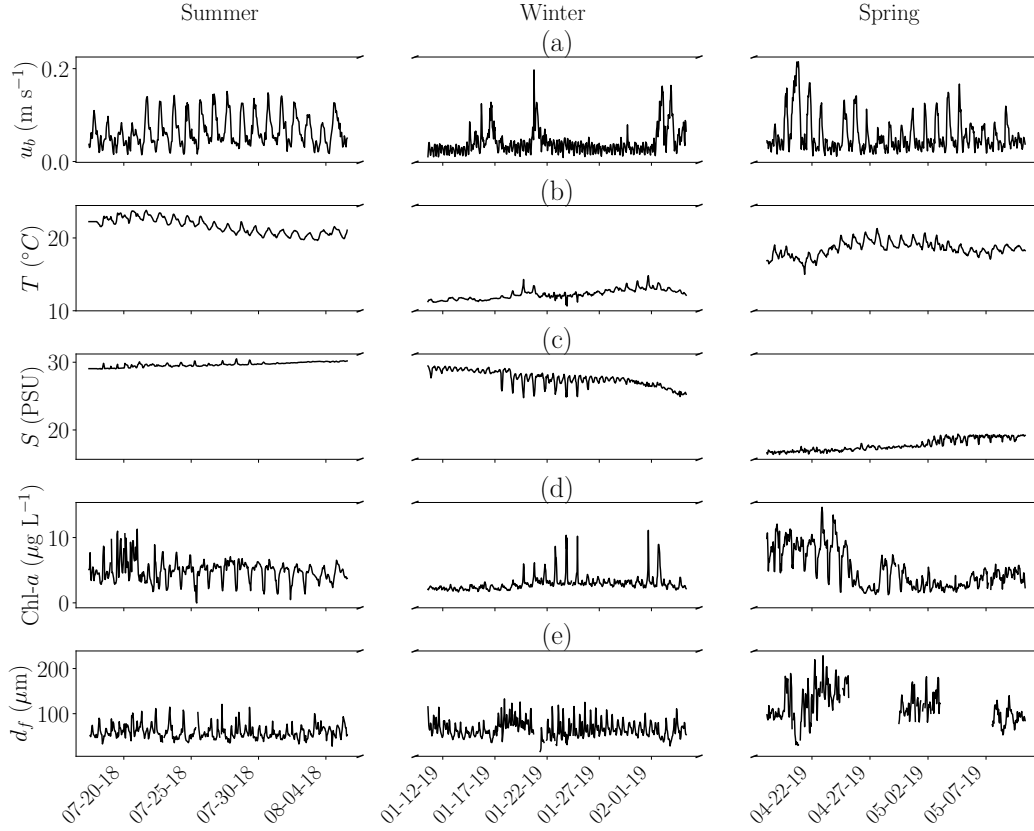


Figure 1: Site conditions for all three field deployments, showing (a) bottom wave-orbital velocity measured by the ADV at 15 cmab, (b) water temperature measured by the CTD at 67 cmab, (c) salinity measured by the CTD at 67 cmab, (d) Chlorophyll-a concentration measured by the fluorometer at 15 cmab, and (e) mean floc size measured by the LISST at 15 cmab.

### 3.2 Suspended sediment regimes

Initial attempts to identify the drivers of particle size variability produced inconclusive results, with trends outweighed by measurement noise. One contributing factor to the noise was inconsistency in the source of suspended sediment at our study site. Figure 2 shows time series of LISST-derived beam attenuation coefficient (a proxy for SSC), along with corresponding measurements of the four-hour lagged mean current velocity at 15 cmab,  $\bar{u}_4$ , and bottom wave-orbital velocity,  $u_b$ . Lagging  $\bar{u}$  by four hours aligns its phase with the water depth, and as seen in Figure 2a, there were periods of our time series when beam attenuation was strongly correlated to  $\bar{u}_4$ , suggesting that the tides advected suspended sediment back and forth across our study site. Interestingly,  $c$  and  $\bar{u}_4$  were often positively correlated, indicating that advected sediment (which increased in concentration during flood tide) was primarily sourced from the channel or deeper shoals to the west of the platform, rather than the shallow shoals to the east. This is somewhat counterintuitive, as the local sediment concentration generally increases eastward due to wave-driven erosion on the shallow shoals. However, tidal currents are also weaker in shallow regions, leading to minimal horizontal transport despite significant local resuspension. Furthermore, the four-hour lag supports the hypothesis of channel-sourced sediment. Platform P1 was located approximately 2.5 km east of the channel, so a four hour transport time would indicate  $17 \text{ cm s}^{-1}$  tidal currents. Depth-averaged ADP measurements at P1 indicate an average eastward flood tide velocity of  $15 \text{ cm s}^{-1}$ , which is consistent with the optimal lag. This trend is also consistent with recent numerical modeling work in South Bay (Chou et al., 2015), which showed enhanced resuspension due to tidal currents during flood tide.

Though the suspended sediment depicted in Figure 2a was likely sourced non-locally, the beam attenuation signal in Figure 2b (measured three days later) was better correlated to the bottom wave-orbital velocity than it was to the tidal current velocity. This correlation suggests that the sediment measured during that time period was primarily suspended from the bed by local wave shear stresses rather than advected to the site from another region. It is reasonable to expect that these two types of suspended sediment—local and non-local—would have different properties, e.g., in terms of size and composition.

In order to elucidate the mechanisms dictating the particle properties, we generalized the results of Figure 2 and split the entire dataset into three regimes: resuspension-

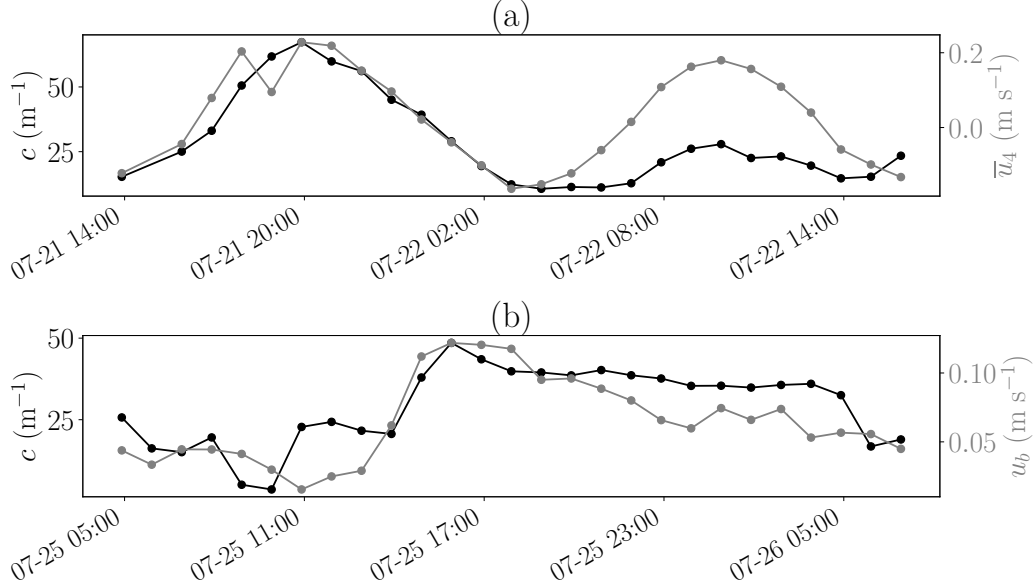


Figure 2: Beam attenuation coefficient ( $c$ , black line) during an (a) advection-driven SSC regime, as shown by the covariation with the four-hour lagged mean current velocity ( $\bar{u}_4$ , gray line), and (b) resuspension-driven SSC regime, as shown by the covariation with the bottom wave-orbital velocity ( $u_b$ , gray line).

dominant (R), advection-dominant (A), and mixed (M, contributions from both). This was accomplished by regressing  $c$  against  $u_b$  and  $\bar{u}_4$  in sliding, forward-looking 12-hour windows. If the coefficient of determination,  $r^2$ , of the linear regression between  $c$  and  $u_b$  was more than 20% larger than  $r^2$  for the linear regression between  $c$  and  $\bar{u}_4$ , then the measurement burst was labeled resuspension-dominant, and vice versa for advection dominant. If the  $r^2$  values for both regressions were within 20% of each other, the measurement burst was labeled as mixed.

For the summer deployment, the regime identification procedure resulted in a resuspension-advection-mixed split of 40.3%(R) – 45.0%(A) – 14.6%(M). The split in winter skewed slightly more toward resuspension (47.4%(R) – 45.3%(A) – 7.4%(M)), while the split in spring was advection-dominant (29.0%(R) – 57.4%(A) – 13.6%(M)). These designations will be used for the remainder of the paper in order to analyze floc behavior within specific suspended sediment regimes.

### 3.3 Particle size variability

To assess which mechanisms exerted the strongest influence on floc size, we carried out a feature selection analysis. A comprehensive overview of feature selection techniques can be found in Guyon and Elisseeff (2003), but in general it refers to the optimization process by which a subset of some large set of independent variables, or “features”, is chosen in order to best predict a dependent variable. In our case, the dependent variable was  $d_f$ , the mean floc diameter, and the full set of independent variables was  $u_b$  (bottom wave-orbital velocity),  $\bar{u}$  (mean current velocity),  $\bar{u}_4$  (four-hour lagged mean current velocity),  $a_{pg}(676)/a_{pg}(650)$  (Chl-*a* absorption spectral peak),  $a_{pg}(450)/a_{pg}(676)$  (detrital/dissolved spectral peak),  $a_{pg}(412)/a_{pg}(650)$  (detrital/dissolved spectral peak), Chl-*a* (Chlorophyll-*a* concentration),  $S$  (salinity),  $T$  (water temperature), and  $\bar{c}$  (mean SSC).

The feature selection was implemented by feeding the output from a LASSO regression (Tibshirani, 1996) into `scikit-learn` RFECV (Pedregosa et al., 2011), an algorithm that recursively eliminates features from the full set, producing a cross-validated subset of features that maximizes the regression coefficient of determination,  $r^2$ . LASSO regression (which is simply ordinary least squares with an  $L^1$ -norm regularization term) is particularly well-suited to feature selection because it encourages a sparse solution, setting regression coefficients for redundant or unhelpful features to zero. We eliminated additional features if their removal from the regression resulted in an  $r^2$  decrease of less than 0.02. This procedure was carried out for the 15 cmab LISST-derived  $d_f$  data during all three deployments and within the three separate suspended sediment regimes discussed in Section 3.2. Results are shown in Table 1.

Across all three deployments,  $d_f$  was predicted with reasonable accuracy ( $r^2 \geq 0.45$ ) in the resuspension regime. In the summer and winter, this was primarily due to a strong negative correlation between floc size and bottom wave-orbital velocity, implying that wave shear stresses were either a) breaking up flocs in the wave bottom boundary layer, or b) resuspending smaller flocs from the bed. Floc size was also positively correlated to  $\bar{u}_4$ , suggesting that even when local shear stress was the dominant source of suspended sediment in the water column, a significant fraction of the advected flocs over the study site during flood tides were larger. In the spring, the negative correlation with wave strength persisted, but the positive correlations to water temperature and chloro-

|     | Resuspension            |               |             | Advection                 |               |             | Mixed                     |               |             |
|-----|-------------------------|---------------|-------------|---------------------------|---------------|-------------|---------------------------|---------------|-------------|
|     | var.                    | $-\Delta r^2$ | (+/-)       | var.                      | $-\Delta r^2$ | (+/-)       | var.                      | $-\Delta r^2$ | (+/-)       |
| Sum |                         |               |             |                           |               |             |                           |               |             |
|     | $u_b$                   | 0.38          | (-)         | $u_b$                     | 0.16          | (-)         | $\bar{u}_4$               | 0.26          | (+)         |
|     | $\bar{u}_4$             | 0.13          | (+)         | $\bar{u}$                 | 0.02          | (+)         | $u_b$                     | 0.17          | (-)         |
|     |                         |               |             |                           |               |             | $\bar{u}$                 | 0.06          | (+)         |
|     |                         |               |             |                           |               |             | $S$                       | 0.03          | (+)         |
|     | <b><math>N</math></b>   |               | <b>179</b>  |                           |               | <b>199</b>  |                           |               | <b>65</b>   |
|     | <b><math>r^2</math></b> |               | <b>0.51</b> |                           |               | <b>0.15</b> |                           |               | <b>0.33</b> |
| Win |                         |               |             |                           |               |             |                           |               |             |
|     | $u_b$                   | 0.26          | (-)         | $\bar{c}$                 | 0.09          | (-)         | $u_b$                     | 0.17          | (-)         |
|     | $\bar{u}_4$             | 0.10          | (+)         | $\bar{u}_4$               | 0.07          | (+)         | $\bar{u}$                 | 0.06          | (-)         |
|     |                         |               |             | $u_b$                     | 0.03          | (-)         | $\bar{u}_4$               | 0.04          | (+)         |
|     |                         |               |             | $\frac{a_{450}}{a_{676}}$ | 0.03          | (+)         | $\frac{a_{676}}{a_{650}}$ | 0.02          | (-)         |
|     |                         |               |             |                           |               |             | Chl- <i>a</i>             | 0.02          | (+)         |
|     | <b><math>N</math></b>   |               | <b>270</b>  |                           |               | <b>258</b>  |                           |               | <b>42</b>   |
|     | <b><math>r^2</math></b> |               | <b>0.45</b> |                           |               | <b>0.50</b> |                           |               | <b>0.65</b> |
| Spr |                         |               |             |                           |               |             |                           |               |             |
|     | $T$                     | 0.42          | (+)         | $T$                       | 0.11          | (+)         | Chl- <i>a</i>             | 0.11          | (+)         |
|     | Chl- <i>a</i>           | 0.23          | (+)         | Chl- <i>a</i>             | 0.09          | (+)         | $T$                       | 0.11          | (+)         |
|     | $u_b$                   | 0.07          | (-)         | $\frac{a_{450}}{a_{676}}$ | 0.03          | (-)         | $\bar{c}$                 | 0.04          | (+)         |
|     |                         |               |             | $\bar{c}$                 | 0.03          | (-)         | $u_b$                     | 0.03          | (-)         |
|     | <b><math>N</math></b>   |               | <b>96</b>   |                           |               | <b>190</b>  |                           |               | <b>45</b>   |
|     | <b><math>r^2</math></b> |               | <b>0.46</b> |                           |               | <b>0.15</b> |                           |               | <b>0.25</b> |

Table 1: Optimal parameters (from top to bottom in order of importance) for predicting  $d_f$  during the summer, winter, and spring deployments. Results are separated by SSC regime, with the total number of data points for the regressions,  $N$ , listed for each regime.  $-\Delta r^2$  indicates the reduction in LASSO total  $r^2$  (shown in bold) that results from removing a particular variable from the regression. (+/-) indicates the sign of the correlation between each variable and  $d_f$ .

334 phyll fluorescence were stronger, indicating a biological control on flocculation during the  
335 spring phytoplankton bloom period.

336 Compared to the resuspension regime, trends in terms of variable importance were  
337 broadly similar in the advection and mixed regimes, with hydrodynamic variables dom-

inating during the summer and winter, and biologically significant variables dominating in the spring. One key difference, however, was that the total regression  $r^2$  was much lower for the advection regime in the summer and spring. Our hypothesis is that if the flocs at our study site originated upstream, then local variables would not be expected to accurately predict the floc properties. Conversely, if the suspended sediment concentration was primarily controlled by local resuspension and settling (i.e., Rouse dynamics), then local hydrodynamic and water quality parameters should be well-correlated to particle properties.

### 3.4 Biological effects

One of the most striking trends from the results in Table 1 was the relative importance of water temperature and chlorophyll fluorescence in predicting floc size during the spring relative to summer and winter. This trend can be examined explicitly through the equilibrium floc size parameterization presented by Winterwerp et al. (2006). Assuming a steady balance between turbulent shear-induced floc breakup and collision-induced aggregation, the equilibrium floc size is given as

$$d_f = \left( \frac{k\bar{c}}{G^q} \right)^{\frac{1}{2q}}, \quad (6)$$

where  $\bar{c}$  is the suspended sediment concentration,  $G = \sqrt{\epsilon/\nu}$  is the turbulent shear rate, and  $k$  is a fitting parameter. The parameter  $q$  is related to the fractal dimension with  $q = \frac{n_f - 1}{2m}$ , where  $m$  is a coefficient that describes how the settling velocity scales with SSC, i.e.,  $w_s \sim \bar{c}^m$ . Setting  $m = 1$  (Winterwerp et al., 2006) and the fractal dimension equal to  $n_f = 2.61$ ,  $n_f = 2.41$ , and  $n_f = 2.11$  for the summer, winter, and spring respectively (Section 3.5), Equation 6 was fit to our data for the resuspension and advection regimes during each deployment using measured values of  $\bar{c}$  and  $G$ . We found that the floc size, and thus the fitting parameter  $k$ , did not vary significantly with SSC. Therefore, we used the mean SSC for each deployment and regime, and regressed for  $d_f$  solely as a function of  $G$ . The result is shown in Figures 3a and 3b.

Between the two regimes,  $r^2$  values were higher in the resuspension regime for the summer and spring, and higher in the advective regime for the winter. Even the best  $r^2$  value, however, was quite poor. Because Equation 6 does not contain an intercept, it is possible to obtain  $r^2 < 0$ . These low coefficients of determination indicate that the equilibrium model does not resolve many of the relevant dynamical processes affecting



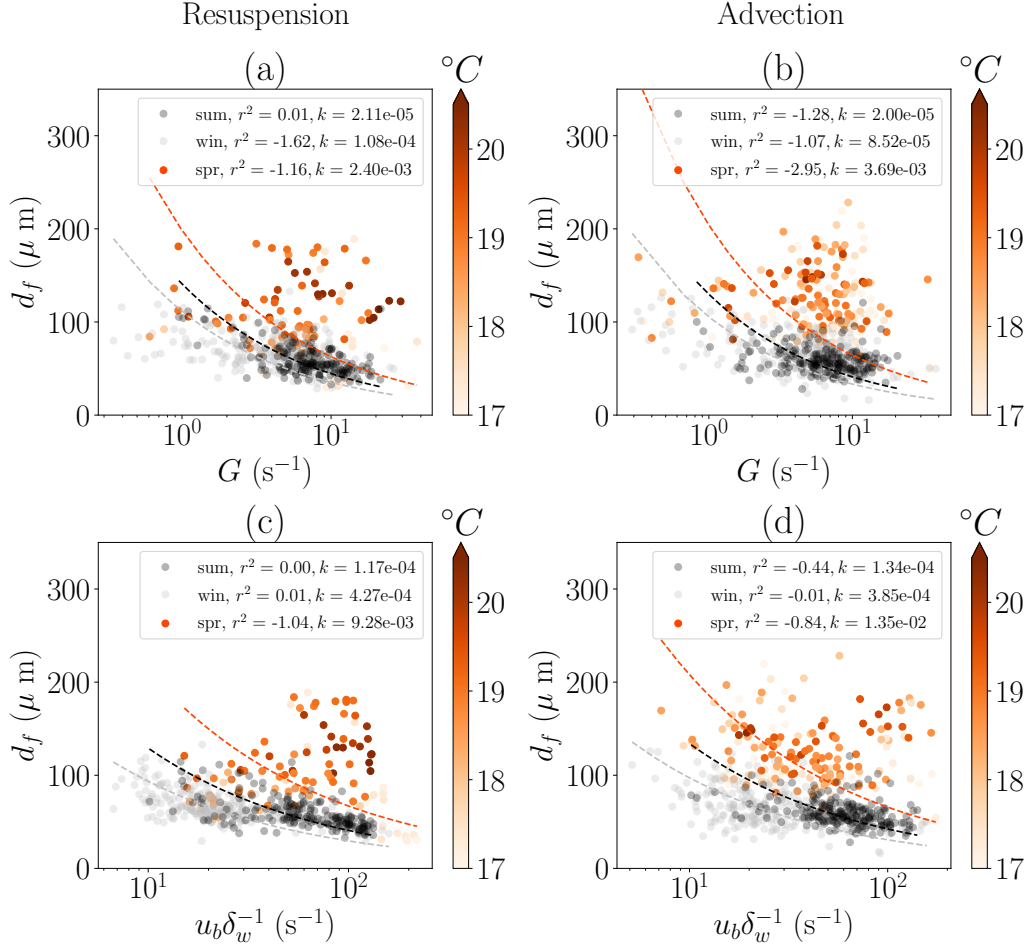


Figure 3: Mean particle diameter as a function of (a) turbulent shear rate in the resuspension regime, (b) turbulent shear rate in the advective regime, (c) wave shear rate in the resuspension regime, and (d) wave shear rate in the advective regime. Data are shown for the summer (black dots), winter (gray dots), and spring deployments (orange dots), with spring data colored by water temperature. The dashed lines show fits to the equilibrium floc size curve (Equation 6), with the fitting parameter  $k$  and coefficient of determination  $r^2$  shown in the legends.

floc size at our study site. This is not surprising, as the dissipation rate of turbulent kinetic energy,  $\epsilon$ , was not selected as an important variable in the LASSO analysis (Table 1). The bottom wave-orbital velocity,  $u_b$ , was generally better-suited to predict floc size. Therefore, in Equation 6 we replaced the turbulent shear rate,  $G$ , with a representative wave shear rate,  $u_b \delta_w^{-1}$ , where  $\delta_w = \sqrt{2\nu/\omega}$  is the Stokes wave boundary layer thickness. Carrying out the equilibrium floc size regression using the wave shear rate resulted in Figures 3c and 3d. Replacing  $G$  with  $u_b \delta_w^{-1}$  improved all but one of the  $r^2$  values, though in general they all remained low. Nevertheless, comparing the fitting parameters between deployments can provide insight into the time-varying particle properties.

The relationship between floc size and both the wave and turbulent shear rates is fairly consistent between the summer and winter deployments, though the optimal  $k$  value is larger during the winter, indicating a modest increase in aggregation potential for a given shear rate. The increase in  $k$  was even larger, however, from winter to spring, and in both regimes a significant number of data points fell above the best-fit line. That trend suggests an additional flocculation mechanism that was present in the spring and absent in the summer and winter. Coloring the spring data by water temperature, many of the larger flocs were measured when the water was relatively warm, which is consistent with the positive correlation between floc size and temperature shown in Table 1.

It is unlikely that water temperature on its own increases the potential for particle aggregation. Water temperatures were higher in the summer compared to the spring, yet there was no relationship between temperature and floc size. Therefore, temperature is likely a proxy for another process that encourages floc growth. For example, laboratory studies have shown that benthic diatoms increase EPS production with increased temperature and irradiance (Wolfstein & Stal, 2002). Maximum water temperatures in our spring data were often measured in the late afternoon, nearing the time of maximum integrated daily irradiance. Therefore, we expect that under conditions favorable to photosynthesis (phytoplankton blooms occur nearly every spring in South San Francisco Bay (Cloern, 1996)), temperature and  $d_f$  were positively correlated because of additional correlations between temperature, irradiance, and EPS production. This hypothesis is probed further in Figure 4, which shows the correlation between temperature and  $d_f$  (parameterized by  $r^2$  from a linear regression) as a function of chlorophyll concentration.

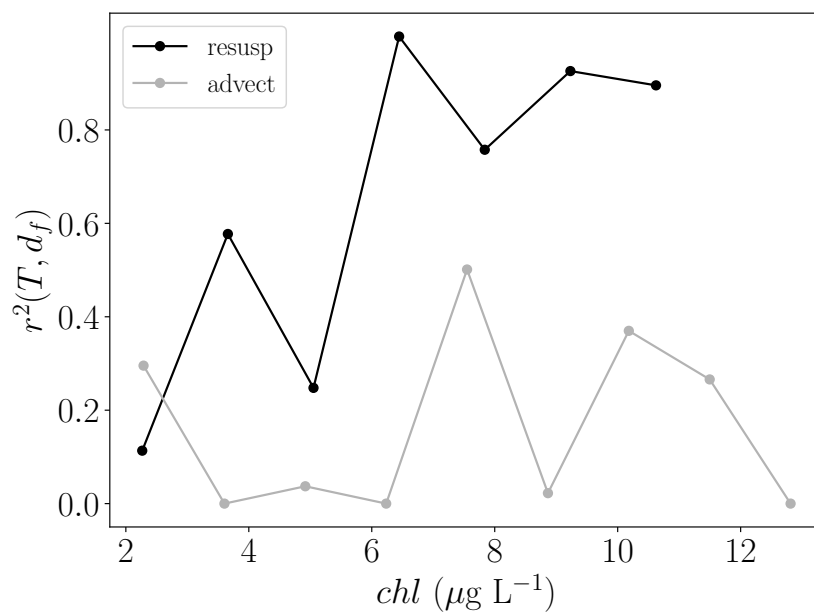


Figure 4: The coefficient of determination from a linear regression between water temperature and mean particle diameter during the spring deployment as a function of chlorophyll concentration. Data are shown in both the resuspension regime (black line) and advective regime (gray line).

In the advective regime, there is no clear trend between  $r^2$  and Chl-*a*. This is expected from Table 1, where the correlation between  $T$  and  $d_f$  was weak to begin with. In the resuspension regime, however,  $r^2$  generally increases with Chl-*a*, peaking at approximately  $6 \mu\text{g L}^{-1}$ . The increase in correlation between  $T$  and  $d_f$  with increasing chlorophyll concentration supports our hypothesis that temperature and floc size are positively correlated due to increased productivity and EPS production that accompany temperature increases. Absent sufficient chlorophyll in the water column, though, increased water temperature will not tend to increase floc size.

### 3.5 Fractal dimension and settling velocity

The results presented so far have focused on the factors driving floc size variability. In the context of sediment transport modeling, however, the floc settling velocity (which is parameterized as a function of floc size) is the most important quantity to constrain. From Equation 3, we see that beyond first-order variability with the shape factor  $\theta$  and size distribution factor  $\phi$ , the settling velocity is controlled primarily by the floc size  $d_f$  and floc fractal dimension  $n_f$ . We initially planned on using INSSEV-LF sampling to determine an appropriate fractal dimension to use in Equation 3. However, logistical constraints limited our INSSEV-LF measurements to one day per deployment, which may not have provided a sufficiently comprehensive view of the monthly (or even diurnally-varying) floc behavior. Nevertheless, the mean fractal dimensions derived from INSSEV-LF data were  $n_f = 2.48$ ,  $n_f = 2.70$ , and  $n_f = 2.66$  for the summer, winter, and spring, respectively. These values are all within the range of previous INSSEV-LF measurements in the region (Manning & Schoellhamer, 2013), though it is surprising that the spring fractal dimension was larger than the summer value, given the substantial evidence of biologically-driven floc growth (e.g., Figures 3 and 4).

As a comparison to the INSSEV-LF results, we followed the methods described by Mikkelsen and Pejrup (2001), who calculated the fractal dimension as  $3+\alpha$ , where  $\alpha$  is the slope of the linear best fit line (in log-log space) between the bin-averaged floc effective density,  $\rho_e$ , as a function of floc size,  $d_f$ . We estimated  $\rho_e$  as

$$\rho_e = \frac{TSM}{VC}, \quad (7)$$

where  $TSM$  is the total suspended matter and  $VC$  is the volume concentration. To improve the measurement fidelity, we estimated both quantities in Equation 7 at the same

location using the same instrument (LISST). The LISST outputs  $VC$  directly, and  $TSM$  was approximated by scaling the beam attenuation,  $c$ , by the linear factor (with appropriate units) for each season that minimized the squared error between  $c$  and  $\bar{c}$ , the acoustic backscatter-derived suspended sediment concentration measured by nearby ADVs. While processing the data, we found that the Mikkelsen and Pejrup (2001) fitting procedure produced far cleaner (higher  $r^2$ ) fits for  $n_f$  when using  $c$  as compared to  $\bar{c}$ . The results of this procedure are shown in Figure 5.

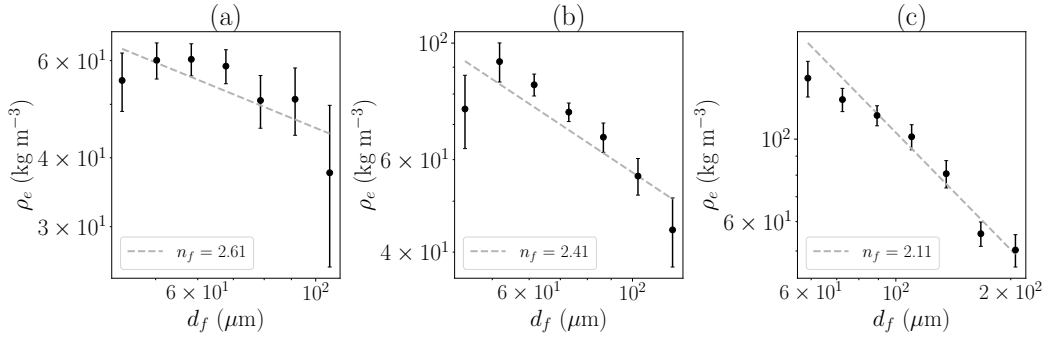


Figure 5: Fractal dimension estimates derived from a linear regression between  $d_f$  and  $\rho_e$  in log-log space for the (a) summer, (b) winter, and (c) spring deployments. Error bars denote the standard error on the bin averaging.

Based on the best-fit slopes in Figure 5, we see a steady decrease in fractal dimension from summer through spring. This indicates that floc structure was closest to that of the primary particles during summer, with more complex flocculation behavior and floc structure during the winter, and especially in the spring. These values are more consistent with the bulk of our results in the sense that they support a lower fractal dimension during the spring productive period. We hypothesize that this was the case because they are derived from hourly LISST data over a month of varying hydrodynamic conditions, rather than the single day of INSSEV-LF sampling during each deployment. Therefore, we incorporated these fractal dimensions into Equation 3 to obtain the settling curves shown in Figure 6. This analysis assumed values of  $\theta = 1$ ,  $\phi = 1$ ,  $d_p = 8\mu\text{m}$  (based on laboratory disaggregated PSD measurements) and  $\rho_p = 2256 \text{ kg m}^{-3}$  (Manning & Dyer, 1999).

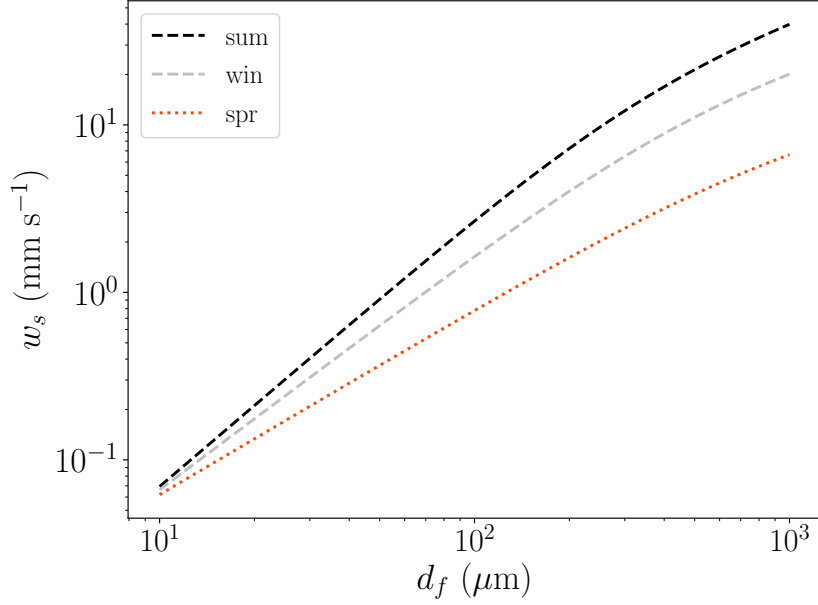


Figure 6: Floc size - settling curves for the summer, winter, and spring based on Equation 3 and the fractal dimensions estimated in Figure 5.

The settling curves demonstrate the importance of considering seasonal variability in fractal dimension. Though the summer and winter settling velocities are similar for a given floc size (within 25% at 100  $\mu\text{m}$ ), the decreased fractal dimension in the spring significantly alters the settling dynamics. For example, a spring floc with a mean diameter of 200  $\mu\text{m}$  (nearly the maximum observed value) would settle with approximately the same velocity as a summer floc with mean diameter 70  $\mu\text{m}$ . Put another way, a spring floc with a mean diameter of 200  $\mu\text{m}$  would settle approximately 4.5 times slower than a summer floc of the same diameter. That magnitude of variability can lead to significant differences in sediment transport modeling results. For example, Allen et al. (2021) demonstrated that a factor of 5 change in settling velocity led to vastly different spatial deposition patterns in a modeling study of San Pablo Bay, a similar environment to our study site. Therefore, our results can provide critical guidance to sediment transport modeling efforts over seasonal timescales.

The settling results also implicitly highlight the key role that sediment plays in nutrient cycling in South San Francisco Bay. Spring flocs, which were likely composed of a significant amount of biological matter, were a key mechanism transporting phytoplank-

ton cells to the sediment bed. Previous work has shown that isolated algal cells settle at rates on the order of  $10^{-3} \text{ mm s}^{-1}$  (Riebesell, 1989). This is approximately three orders of magnitude slower than a  $200 \text{ }\mu\text{m}$  floc during the spring, as seen in Figure 6. Such a vast difference in vertical settling rate would have a profound effect on any biogeochemical modeling effort, showing the importance of resolving flocculation dynamics for a wide range of estuarine process studies.

### 3.6 Implications for inverse turbulent Schmidt number

One challenge in analyzing the inverse turbulent Schmidt number ( $\beta$ , Equations 4 and 5) as a function of floc size is the fact that the LISST data were collected at 15 cmab, while the Vectrino sampled from 0–1.5 cmab where the turbulence statistics and particle properties were likely different. To account for this discrepancy, we nondimensionalized floc size by the Kolmogorov length scale,  $\eta = (\nu^3 \epsilon^{-1})^{1/4}$ , using the dissipation rate at 15 cmab. This should allow for a more general examination of how sediment diffusivity varies with floc size for a given level of turbulence. The result of this analysis, conducted for both the summer and spring deployments, is shown in Figure 7.

The inverse turbulent Schmidt number was approximately equal to unity for the smallest flocs sampled during the summer, indicating that the turbulent sediment diffusivity was equal to the turbulent momentum diffusivity, i.e., the flocs acted as flow tracers. In the limit of vanishingly small flocs, this is an intuitive result, as the Stokes number associated with the particles goes to zero. As the relative floc size increases, however,  $\beta$  decreases before leveling off near  $\beta \approx 0.3$ . The negative correlation between  $\beta$  and  $d_f \eta^{-1}$  can be explained as a consequence of faster settling by larger flocs, which would be expected given the dense, minerogenic floc populations we sampled in the summer (Section 3.5). Faster settling increases the near-bed concentration gradient relative to the turbulent sediment flux (numerator of Equation 5), so it follows that  $\beta$  decreases with increased floc size.

Interestingly, the spring data show a different trend. Though the inverse turbulent Schmidt number decreases slightly with normalized floc size, the slope of the trend is statistically indistinguishable from zero. The flocs were also much larger (maximum near  $0.8\eta$  rather than  $0.3\eta$ ), yet  $\beta \approx 1$  throughout the range of floc size. This relatively con-

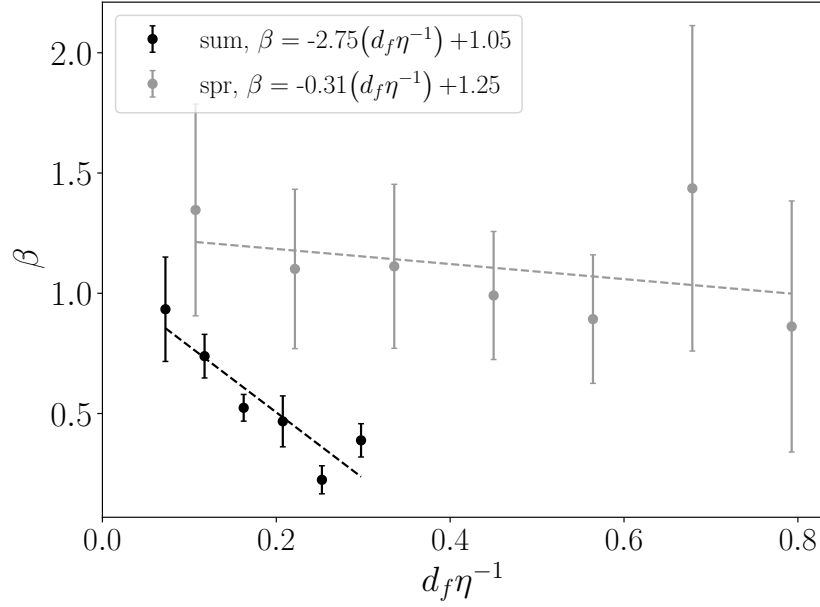


Figure 7: The inverse turbulent Schmidt number (Equations 4 and 5) bin-averaged by the nondimensional floc diameter. Data are separated by summer (black dots) and spring deployments (gray dots), with linear regressions denoted by the dashed lines and associated equations in the legend. Error bars denote the standard error on the bin-averaging.



stant diffusivity could be caused by the flocs having lower density in the spring, which could counter increased settling rates despite the increased particle size. Such an effect would allow the spring flocs to follow the turbulent flow more effectively than the dense summer flocs.

Though Figure 7 suggests a strong relationship between floc size and Schmidt number, causation is difficult to prove. There are numerous physical phenomena in this system that are correlated to  $d_f\eta^{-1}$  which may also contribute to variability in  $\beta$ . Therefore, it is critical to rule out possible mechanisms that could lead to a similar trend. First examining sediment-induced stratification: all things being equal, increased settling velocity tends to strengthen sediment-induced stratification. Stronger stratification could then further increase  $d_f\eta^{-1}$  by reducing both  $\eta$  and turbulence-induced floc breakup. However, the near-bed turbulent eddy viscosity (denominator of Equation 4) would decrease as stratification intensifies, causing a corresponding increase in  $\beta$ . This is the opposite trend compared to Figure 7, indicating that the results cannot be explained by stratification.

Another mechanism that could explain our results is wave-induced  $\beta$  variability. Stronger waves tend to reduce floc size (Table 1) while increasing the turbulent sediment flux relative to the turbulent momentum flux (Egan et al., 2021), a combination that could cause the negative correlation between  $\beta$  and  $d_f\eta^{-1}$  seen in Figure 7. To further examine this possibility, we separated our dataset into three regimes of wave strength parameterized by the wave Reynolds number,

$$\text{Re}_w = \frac{u_b a_b}{\nu}, \quad (8)$$

where  $a_b = u_b\omega^{-1}$  is the wave orbital excursion. The wave regimes were determined such that there was an equal number of data points in each category (Low, Medium, and High) for each season. During both summer and spring,  $\text{Re}_w$  values ranged from  $\mathcal{O}(10^2)$ – $\mathcal{O}(10^4)$ . An analogous binning between  $\beta$  and  $d_f\eta^{-1}$  was then carried out for the individual wave strength regimes, as shown in Figure 8.

During the summer, stronger waves do tend to increase  $\beta$  for a given  $d_f\eta^{-1}$ , as we hypothesized. Yet across  $\text{Re}_w$  regimes, the trends in Figure 8 are not appreciably different from Figure 7, showing a negative correlation between  $\beta$  and  $d_f\eta^{-1}$  in the summer and an approximately constant  $\beta$  with normalized floc size in the spring (within uncer-

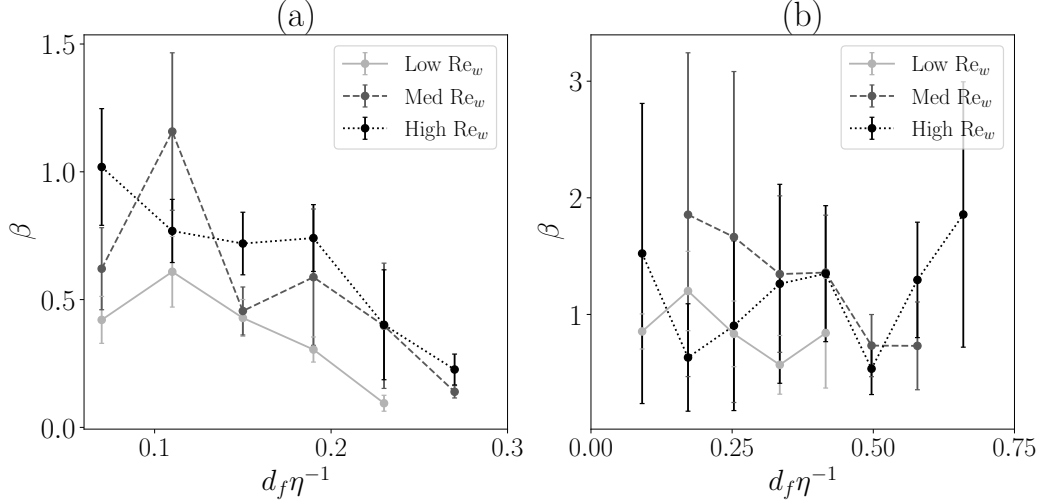


Figure 8: The inverse turbulent Schmidt number (Equations 4 and 5) bin-averaged by the nondimensional floc diameter during the (a) summer and (b) spring deployments. Data are separated by low  $Re_w$  (light gray), medium  $Re_w$  (dark gray dashed), and high  $Re_w$  conditions (black dotted). Error bars denote the standard error on the bin-averaging.

515 tainty). Critically, the trends within each wave regime show stronger variability than the  
 516 differences among the wave regimes during the summer. Given that wave strength was  
 517 the primary driver of summer floc size variability (Table 1), this deconstructed view sup-  
 518 ports the hypothesis that  $d_f \eta^{-1}$  contributes to the dynamics of turbulent sediment dif-  
 519 fusion.

520 In the context of numerical sediment transport modeling, the results in Figures 7  
 521 and 8 suggest that an inverse turbulent Schmidt number value of  $\beta \approx 1$  is appropri-  
 522 ate for a wide range of floc sizes when the floc composition is influenced by water col-  
 523 umn biology. For denser flocs,  $\beta \approx 1$  may be reasonable for the smallest floc sizes, with  
 524 a decrease towards a minimum of  $\beta \approx 0.3$  as  $d_f \eta^{-1}$  increases. The slope of the decrease  
 525 is shown in the Figure 7 legend, though we are not suggesting that the trend be extrap-  
 526 olated beyond the maximum floc sizes we measured.

## 527 4 Conclusions

528 The results presented here provide an assessment of the factors driving cohesive  
 529 sediment floc size variability in estuarine environments. During time periods character-

ized largely by minerogenic sediments, flocc size was negatively correlated to wave strength, indicating that wave shear stress in the bottom boundary layer can be a powerful mechanism encouraging flocc breakup. During the spring productive period when flocc size was generally larger, we found strong correlations between temperature and flocc size. We hypothesize that temperature was a proxy measurement indicative of biological processes (e.g., EPS production) that would promote flocc growth. These seasonal trends were reflected in both settling velocity and inverse turbulent Schmidt number estimates, both of which are critical parameters for accurately representing cohesive sediment in numerical sediment transport models (Celik & Rodi, 1988).

The interplay between biology and flocc size had a profound impact on flocc settling velocity and turbulence dynamics. Between the summer and spring deployments, variations in flocc composition led to a nearly five-fold increase in settling velocity for a given flocc size (Figure 6). This level of variability presents an enormous challenge for sediment transport modeling efforts, where settling velocity must be accurately prescribed in order to represent spatially-varying settling and depositional phenomena. We also found seasonal differences in the relationship between normalized flocc size and inverse turbulent Schmidt number (Figure 7). Increases in  $d_f \eta^{-1}$  during the summer resulted in significant decreases in  $\beta$ , which we hypothesized was caused by faster settling of dense, minerogenic floccs. In contrast,  $\beta$  showed little variability with  $d_f \eta^{-1}$  during the spring when floccs were primarily biological in origin.

Finally, the novel quantitative tools used for these analyses can likely be applied in a broad range of estuarine studies. For example, when separated by source (advection vs resuspension-driven), we found that LASSO regression can be a powerful tool for identifying the variables that influence flocc breakup and growth under a wide range of physical, chemical, and biological forcing conditions. Sediment data are notoriously noisy, and cohesive sediment data particularly so, as flocc characteristics (size and composition) can change dramatically over timescales on the order of minutes. Nevertheless, high-dimensional regression techniques are able to identify robust trends in these datasets. As discussed in the recent review by Goldstein et al. (2019), machine learning techniques are increasingly providing insight into sediment dynamics, and may be a fruitful area of future study.

## Acknowledgments

G. Egan gratefully acknowledges the support of the Charles H. Leavell Graduate Fellowship. This work was funded by the US National Science Foundation under grant OCE-1736668. We thank Frank Spada, Kara Scheu, Marianne Cowherd, Stephen LaMothe, and Jim Christmann for their assistance with the field work. All data used in this publication can be found at <https://purl.stanford.edu/wv787xr0534> and <https://purl.stanford.edu/sh883gp0753>

## References

- Agrawal, Y. C., & Pottsmith, H. C. (2000). Instruments for particle size and settling velocity observations in sediment transport. *Marine Geology*, 168(1-4), 89–114.
- Allen, R. M., Lacy, J. R., & Stevens, A. W. (2021). Cohesive sediment modeling in a shallow estuary: Model and environmental implications of sediment parameter variation. *Journal of Geophysical Research: Oceans*, 126(9), e2021JC017219.
- Boss, E., & Pegau, W. S. (2001). Relationship of light scattering at an angle in the backward direction to the backscattering coefficient. *Applied Optics*, 40(30), 5503–5507.
- Boss, E., Sherwood, C. R., Hill, P., & Milligan, T. (2018). Advantages and limitations to the use of optical measurements to study sediment properties. *Applied Sciences*, 8(12), 2692.
- Brand, A., Lacy, J. R., Hsu, K., Hoover, D., Gladding, S., & Stacey, M. T. (2010). Wind-enhanced resuspension in the shallow waters of south san francisco bay: Mechanisms and potential implications for cohesive sediment transport. *Journal of Geophysical Research: Oceans*, 115(C11).
- Bricker, J. D., & Monismith, S. G. (2007). Spectral wave–turbulence decomposition. *Journal of Atmospheric and Oceanic Technology*, 24(8), 1479–1487.
- Celik, I., & Rodi, W. (1988). Modeling suspended sediment transport in nonequilibrium situations. *Journal of Hydraulic Engineering*, 114(10), 1157–1191.
- Chou, Y.-J., Holleman, R. C., Fringer, O. B., Stacey, M. T., Monismith, S. G., & Koseff, J. R. (2015). Three-dimensional wave-coupled hydrodynamics modeling in south san francisco bay. *Computers & Geosciences*, 85, 10–21.
- Cloern, J. E. (1996). Phytoplankton bloom dynamics in coastal ecosystems: a review with some general lessons from sustained investigation of san francisco bay,

- california. *Reviews of Geophysics*, *34*(2), 127–168.
- Dyer, K. (1989). Sediment processes in estuaries: future research requirements. *Journal of Geophysical Research: Oceans*, *94*(C10), 14327–14339.
- Dyer, K., & Manning, A. (1999). Observation of the size, settling velocity and effective density of flocs, and their fractal dimensions. *Journal of sea research*, *41*(1-2), 87–95.
- Egan, G., Chang, G., McWilliams, S., Revelas, G., Fringer, O., & Monismith, S. (2021). Cohesive sediment erosion in a combined wave-current boundary layer. *Journal of Geophysical Research: Oceans*, *126*(2), e2020JC016655.
- Egan, G., Chang, G., Revelas, G., Monismith, S., & Fringer, O. (2020). Bottom drag varies seasonally with biological roughness. *Geophysical Research Letters*, *47*(15), e2020GL088425.
- Egan, G., Cowherd, M., Fringer, O., & Monismith, S. (2019). Observations of near-bed shear stress in a shallow, wave-and current-driven flow. *Journal of Geophysical Research: Oceans*, *124*(8), 6323–6344.
- Egan, G., Manning, A. J., Chang, G., Fringer, O., & Monismith, S. (2020). Sediment-induced stratification in an estuarine bottom boundary layer. *Journal of Geophysical Research: Oceans*, *125*(8), e2019JC016022.
- Eisma, D. (1986). Flocculation and de-flocculation of suspended matter in estuaries. *Netherlands Journal of Sea Research*, *20*(2-3), 183–199.
- Goldstein, E. B., Coco, G., & Plant, N. G. (2019). A review of machine learning applications to coastal sediment transport and morphodynamics. *Earth-science reviews*, *194*, 97–108.
- Gualtieri, C., Angeloudis, A., Bombardelli, F., Jha, S., & Stoesser, T. (2017). On the values for the turbulent schmidt number in environmental flows. *Fluids*, *2*(2), 17.
- Guyon, I., & Elisseff, A. (2003). An introduction to variable and feature selection. *Journal of machine learning research*, *3*(Mar), 1157–1182.
- Heffler, D., Syvitski, J., & Asprey, K. (1991). The flocc camera. *Principles, methods, and application of particle size analysis*, 209–221.
- Hill, P. S., Milligan, T. G., & Geyer, W. R. (2000). Controls on effective settling velocity of suspended sediment in the eel river flood plume. *Continental shelf research*, *20*(16), 2095–2111.

- 625 Hill, P. S., Syvitski, J. P., Cowan, E. A., & Powell, R. D. (1998). In situ observations  
626 of flocc settling velocities in glacier bay, alaska. *Marine Geology*, 145(1-2), 85–  
627 94.
- 628 James, S. C., Jones, C. A., Grace, M. D., & Roberts, J. D. (2010). Advances in sedi-  
629 ment transport modelling. *Journal of Hydraulic Research*, 48(6), 754–763.
- 630 Khelifa, A., & Hill, P. S. (2006). Models for effective density and settling velocity of  
631 floccs. *Journal of Hydraulic Research*, 44(3), 390–401.
- 632 Koca, K., Noss, C., Anlanger, C., Brand, A., & Lorke, A. (2017). Performance of the  
633 vectrino profiler at the sediment–water interface. *Journal of Hydraulic Research*,  
634 55(4), 573–581.
- 635 Kolmogorov, A. N. (1941). The local structure of turbulence in incompressible viscous  
636 fluid for very large reynolds numbers. *Cr Acad. Sci. URSS*, 30, 301–305.
- 637 Kranenburg, C. (1994). The fractal structure of cohesive sediment aggregates. *Estuar-  
638 ine, Coastal and Shelf Science*, 39(6), 451–460.
- 639 Lees, B. (1981). Relationship between eddy viscosity of seawater and eddy diffusivity  
640 of suspended particles. *Geo-Marine Letters*, 1(3-4), 249–254.
- 641 Lick, W. (2008). *Sediment and contaminant transport in surface waters*. CRC press.
- 642 Manning, A., & Bass, S. J. (2006). Variability in cohesive sediment settling fluxes:  
643 Observations under different estuarine tidal conditions. *Marine Geology*, 235(1-  
644 4), 177–192.
- 645 Manning, A., & Dyer, K. (1999). A laboratory examination of flocc characteristics with  
646 regard to turbulent shearing. *Marine Geology*, 160(1-2), 147–170.
- 647 Manning, A., Friend, P., Prowse, N., & Amos, C. (2007). Preliminary findings from a  
648 study of medway estuary (uk) natural mud flocc properties using a laboratory  
649 mini-flume and the labsfloc system. *Continental Shelf Research, BIOFLOW SI*,  
650 1080–1095.
- 651 Manning, A., & Schoellhamer, D. (2013). Factors controlling flocc settling velocity  
652 along a longitudinal estuarine transect. *Marine Geology*, 345, 266–280.
- 653 Manning, A., Whitehouse, R., & Uncles, R. (2017). Suspended particulate matter: the  
654 measurements of floccs. *ECOA practical handbooks on survey and analysis meth-  
655 ods: Estuarine and coastal hydrography and sedimentology*, 211–260.
- 656 McCave, I. (1984). Size spectra and aggregation of suspended particles in the deep  
657 ocean. *Deep Sea Research Part A. Oceanographic Research Papers*, 31(4), 329–

352.

- Mehta, A. J., Manning, A. J., & Khare, Y. P. (2014). A note on the krone deposition equation and significance of flocc aggregation. *Marine Geology*, *354*, 34–39.
- Mietta, F., Chassagne, C., Manning, A., & Winterwerp, J. (2009). Influence of shear rate, organic matter content, ph and salinity on mud flocculation. *Ocean Dynamics*, *59*(5), 751–763.
- Mikkelsen, O., & Pejrup, M. (2001). The use of a lisst-100 laser particle sizer for in-situ estimates of floc size, density and settling velocity. *Geo-Marine Letters*, *20*(4), 187–195.
- Milligan, T. (1996). In situ particle (floc) size measurements with the benthos plankton silhouette camera. *Journal of Sea Research*, *36*(1-2), 93–100.
- Pedregosa, F., Varoquaux, G., Gramfort, A., Michel, V., Thirion, B., Grisel, O., . . . Duchesnay, E. (2011). Scikit-learn: Machine learning in Python. *Journal of Machine Learning Research*, *12*, 2825–2830.
- Prandle, D., & Lane, A. (2015). Sensitivity of estuaries to sea level rise: vulnerability indices. *Estuarine, Coastal and Shelf Science*, *160*, 60–68.
- Riebesell, U. (1989). Comparison of sinking and sedimentation rate measurements in a diatom winter/spring bloom. *Marine Ecology Progress Series*, *54*, 109–119.
- Roesler, C. S., Perry, M. J., & Carder, K. L. (1989). Modeling in situ phytoplankton absorption from total absorption spectra in productive inland marine waters. *Limnology and Oceanography*, *34*(8), 1510–1523.
- Smith, S. J., & Friedrichs, C. T. (2011). Size and settling velocities of cohesive flocs and suspended sediment aggregates in a trailing suction hopper dredge plume. *Continental Shelf Research*, *31*(10), S50–S63.
- Smith, S. J., & Friedrichs, C. T. (2015). Image processing methods for in situ estimation of cohesive sediment floc size, settling velocity, and density. *Limnology and Oceanography: Methods*, *13*(5), 250–264.
- Son, M., & Hsu, T.-J. (2011). The effects of flocculation and bed erodibility on modeling cohesive sediment resuspension. *Journal of Geophysical Research: Oceans*, *116*(C3).
- Soulsby, R., Manning, A., Spearman, J., & Whitehouse, R. (2013). Settling velocity and mass settling flux of flocculated estuarine sediments. *Marine Geology*, *339*, 1–12.

- Spencer, K. L., Wheatland, J. A., Bushby, A. J., Carr, S. J., Droppo, I. G., & Manning, A. J. (2021). A structure–function based approach to floc hierarchy and evidence for the non-fractal nature of natural sediment flocs. *Scientific reports*, *11*(1), 1–10.
- Stokes, G. G., et al. (1851). *On the effect of the internal friction of fluids on the motion of pendulums* (Vol. 9). Pitt Press Cambridge.
- Stolzenbach, K. D., & Elimelech, M. (1994). The effect of particle density on collisions between sinking particles: implications for particle aggregation in the ocean. *Deep Sea Research Part I: Oceanographic Research Papers*, *41*(3), 469–483.
- Sullivan, J. M., Twardowski, M. S., Zaneveld, J. R. V., Moore, C. M., Barnard, A. H., Donaghay, P. L., & Rhoades, B. (2006). Hyperspectral temperature and salt dependencies of absorption by water and heavy water in the 400–750 nm spectral range. *Applied Optics*, *45*(21), 5294–5309.
- Syvitski, J. P., & Hutton, E. W. (1996). In situ characteristics of suspended particles as determined by the floc camera assembly fca. *Journal of Sea Research*, *36*(1–2), 131–142.
- Tibshirani, R. (1996). Regression shrinkage and selection via the lasso. *Journal of the Royal Statistical Society: Series B (Methodological)*, *58*(1), 267–288.
- Tolhurst, T., Gust, G., & Paterson, D. (2002). The influence of an extracellular polymeric substance (eps) on cohesive sediment stability. In *Proceedings in marine science* (Vol. 5, pp. 409–425). Elsevier.
- Van Leussen, W. (1997). The kolmogorov microscale as a limiting value for the floc sizes of suspended fine-grained sediments in estuaries. *Cohesive sediments*, 45–62.
- Verney, R., Lafite, R., & Brun-Cottan, J.-C. (2009). Flocculation potential of estuarine particles: The importance of environmental factors and of the spatial and seasonal variability of suspended particulate matter. *Estuaries and coasts*, *32*(4), 678–693.
- Vowinckel, B., Withers, J., Luzzatto-Fegiz, P., & Meiburg, E. (2019). Settling of cohesive sediment: particle-resolved simulations. *Journal of Fluid Mechanics*, *858*, 5–44.
- Winterwerp, J. (1998). A simple model for turbulence induced flocculation of cohesive sediment. *Journal of hydraulic research*, *36*(3), 309–326.



- 724 Winterwerp, J. (2002). On the flocculation and settling velocity of estuarine mud.  
725 *Continental shelf research*, 22(9), 1339–1360.
- 726 Winterwerp, J., Manning, A., Martens, C., De Mulder, T., & Vanlede, J. (2006). A  
727 heuristic formula for turbulence-induced flocculation of cohesive sediment. *Es-*  
728 *tuarine, Coastal and Shelf Science*, 68(1-2), 195–207.
- 729 Wolfstein, K., & Stal, L. J. (2002). Production of extracellular polymeric substances  
730 (eps) by benthic diatoms: effect of irradiance and temperature. *Marine Ecology*  
731 *Progress Series*, 236, 13–22.
- 732 Zaneveld, J. R., & Pegau, W. (1993). Temperature-dependent absorption of water in  
733 the red and near-infrared portions of the spectrum.
- 734 Zhang, X., Hu, L., & He, M.-X. (2009). Scattering by pure seawater: effect of salinity.  
735 *Optics express*, 17(7), 5698–5710.